THE JOURNAL OF PHYSICAL CHEMISTRY B

Article

pubs.acs.org/JPCB

Revisiting Photoemission and Inverse Photoemission Spectra of Nickel Oxide from First Principles: Implications for Solar Energy Conversion

Nima Alidoust,[†] Maytal Caspary Toroker,[‡] and Emily A. Carter*,[§]

[†]Department of Electrical Engineering, Princeton University, Princeton, New Jersey 08544-5263, United States

[‡]Department of Materials Science and Engineering, Technion - Israel Institute of Technology, Haifa 32000, Israel

[§]Department of Mechanical and Aerospace Engineering, Program in Applied and Computational Mathematics, and Andlinger Center for Energy and the Environment, Princeton University, Princeton, New Jersey 08544-5263, United States

ABSTRACT: We use two different ab initio quantum mechanics methods, complete active space self-consistent field theory applied to electrostatically embedded clusters and periodic many-body G_0W_0 calculations, to reanalyze the states formed in nickel(II) oxide upon electron addition and ionization. In agreement with interpretations of earlier measurements, we find that the valence and conduction band edges consist of oxygen and nickel states, respectively. However, contrary to conventional wisdom, we find that the oxygen states of the valence band edge are *localized* whereas the nickel states at the conduction band edge are *delocalized*. We argue that these characteristics may lead to low electron−hole recombination and relatively efficient electron transport, which, coupled with band gap engineering, could produce higher solar energy conversion efficiency compared to that of other transition-metal oxides. Both methods find a photoemission/inverse-photoemission gap of 3.6−3.9 eV, in good agreement with the experimental range, lending credence to our analysis of the electronic structure of NiO.

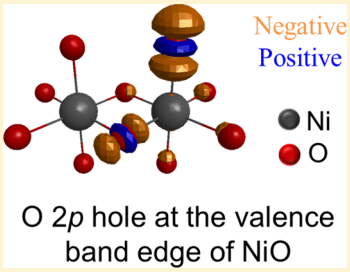

INTRODUCTION

The demand for inexpensive and efficient alternative materials for converting solar energy to electricity and fuel has sparked interest in materials based on first-row transition-metal oxides (TMOs). Many investigations have studied titanium dioxide (TiO_2) as a photoanode in photoelectrochemical cells and dye-sensitized solar cells.[1] Hematite (α-Fe_2O_3) also has potential as a photoanode because of its stability and sufficient light absorption.[2] Another promising TMO is nickel(II) oxide (NiO), the most stable oxide of the inexpensive, abundant element Ni, already in widespread use in solar energy applications.[3−10] NiO is used in polymer-based heterojunction solar cells as an efficiency-enhancing interfacial layer.[4] Doping $InTaO_4$ with Ni, along with forming a partially oxidized Ni surface, produces a photocatalyst for water-splitting.[6] NiO is also deployed extensively in *p*-type and tandem dye-sensitized solar cells.[5,7,11−16] The potential use of NiO for solar energy conversion could expand even further if one considers measurements identifying NiO as a charge-transfer (CT) semiconductor.[17] The latter property means that the valence band edge (VBE) and conduction band edge (CBE) of NiO consist of O and Ni states, respectively. Such a feature has been proposed to potentially enhance intersystem crossing between nearly degenerate excited states of different spin, and thereby increase the lifetime of the photoexcited carriers.[18]

Despite these favorable properties, state-of-the-art NiO-based devices suffer from low efficiencies. Theoretical modeling can help suggest ways to optimize the electronic structure of NiO to overcome this deficiency. A well-suited theory for this purpose has to meet three important criteria: (i) agreement with experiment when describing the band gap and characters of the VBE and CBE of pure NiO; (ii) full ab initio formulation, avoiding empirical or adjustable parameters, as these limit predictive capability; and (iii) going beyond ground electronic state calculations to compare with measurements. Most previous attempts to characterize the electronic structure of NiO fall short on at least one of these criteria.[17,19−27]

Early ground-state theories failed to give a qualitatively consistent picture of NiO electronic structure when compared to experiment. One-electron band theory predicts NiO to be a conductor with no gap because Ni 3d (e_g) orbitals are half-filled. However, photoemission spectroscopy (PES) and inverse-photoemission spectroscopy (IPES) experiments measure gaps ranging from 3.4 to 4.6 eV for NiO.[17,28] To resolve this inconsistency, Mott and Hubbard interpreted the band gap of NiO as a splitting between Ni d bands arising from the strong Coulomb interaction between the localized d electrons.[20,21] However, experiments revealed that O 2p states have a strong presence at the VBE.[29] Density functional theory (DFT) in the local-spin-density approximation (LSDA) does not resolve this inconsistency. It yields a small band gap, with prominent Ni 3d character in both the VBE and CBE.[22] The root of such a large underestimation of the gap is the self-

Special Issue: James L. Skinner Festschrift

Received: January 24, 2014
Revised: March 30, 2014
Published: April 1, 2014

   dx.doi.org/10.1021/jp500878s | *J. Phys. Chem. B* 2014, 118, 7963−7971

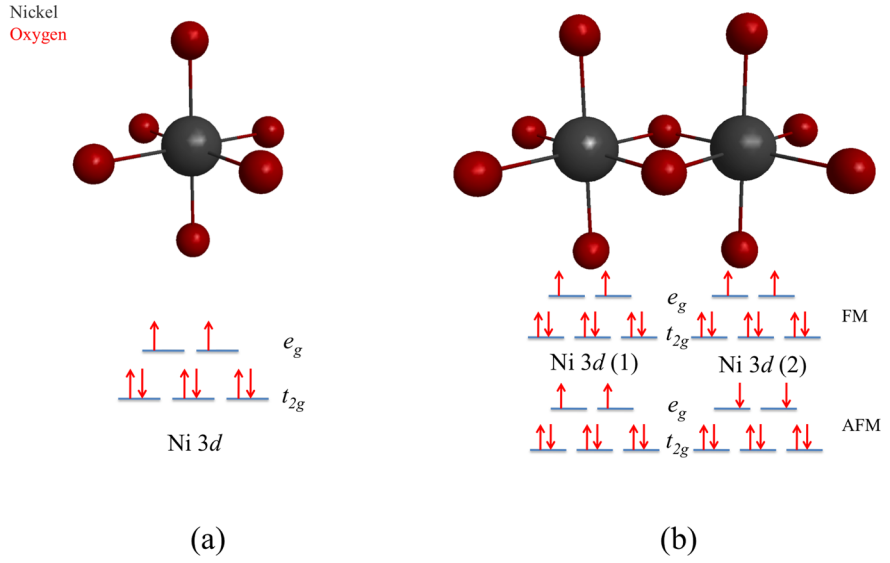

Figure 1. (a) Electrostatically embedded $[NiO_6]^{10-}$ and (b) $[Ni_2O_{10}]^{16-}$ clusters used in calculating PES and IPES energy levels of NiO, along with a schematic representation of the ground-state configuration of electrons in Ni 3d orbitals. Embedding ions and effective core potentials are not shown for ease of viewing. Octahedral crystal field splitting causes the 3d orbitals on Ni^{2+} ions to split into t_{2g} and e_g levels. In the ground state, the O 2p orbitals are all doubly occupied (not shown). Configuration (b) shows both ferromagnetic (FM) and antiferromagnetic (AFM) couplings of two neighboring Ni ions. Both of these configurations occur in NiO crystal, which has AFM ordering in the [111] direction and FM ordering in the (111) planes.[46,47]

interaction error inherent in standard DFT approximations. The 3d orbitals of Ni^{2+} ions are highly localized and host a significant number of open-shell electrons. This gives rise to large Coulomb and exchange energies. However, because the exchange−correlation (XC) functionals used in DFT are approximate, they fail to exactly cancel the spurious self-interaction energy caused by each electron being repelled by its own mean-field contribution to the Coulomb energy. This leads to an unphysical repulsion of each electron by its own charge, which delocalizes the electrons and artificially brings down the gap. The DFT-based DFT+U method removes self-interaction error by introducing Hartree−Fock (HF)-like average Coulomb (U) and exchange (J) energies to treat the intra-atomic Ni 3d electronic interactions. As the $U - J$ value (the relevant parameter in DFT+U) increases, O 2p states start to appear at the VBE and the gap widens.[23−25] Despite this improvement, DFT+U is still a ground-state theory. Hence, the resulting electronic structure cannot be compared directly to measurements such as PES and IPES. For such comparisons, higher levels of theory, such as the many-body Green's function theory GW[30] and configuration interaction (CI),[31] are needed.

GW calculates the quasiparticle (QP) gap, which is directly comparable to PE and IPE spectra. It is performed as a perturbation on one-electron eigenvalues and wave functions of ground-state theories such as pure DFT, DFT+U, or hybrid DFT, e.g., with the Heyd−Scuseria−Ernzerhof (HSE) hybrid functional[32,33] (denoted herein as DFT/GW, DFT+U/GW, and HSE/GW). Previous GW calculations on NiO predict a variety of QP gaps. Non-self-consistent GW (G_0W_0) using input from DFT+U with the local density approximation (LDA) for the XC functional and a $U - J$ value of 4.3 eV results in a QP gap of 3.8 eV,[34] whereas hybrid-DFT/G_0W_0 calculations based on the HSE functional predict a QP gap of 4.7 eV.[35] The QP gap resulting from QP self-consistent GW (QP-$scGW$) is 4.8 eV.[36] The latter two calculations slightly overestimate the gap, while the first calculation determines U and J values for the DFT+U calculation using the constrained DFT approach,[37] which uses an approximate XC functional and is therefore subject to errors.

Other attempts to go beyond ground-state theories include CI calculations on small clusters in the 1980s by Fujimori and Minami,[26] and Anderson impurity model calculations by Zaanen et al.[27] These calculations determined the PES main peak to be due to a $d^8L \rightarrow d^8\underline{L}$ transition, where $\underline{L}$ represents a hole on the ligand. Fujimori and Minami[26] further characterized the hole left behind after ionization as electron removal first from Ni 3d (t_{2g}), followed by a transition from O 2p to Ni 3d (t_{2g}). However, these decades-old calculations are not expected to be entirely reliable. First, to minimize computational expense, the molecular orbitals in the CI calculations were frozen at a lower level self-consistent-field (SCF) theory, meaning that the orbitals could not change their shapes after removing (or adding) an electron in the PES (IPES) processes. This may be an appropriate approximation under certain circumstances (e.g., neutral optical excitations); however, such orbital relaxations generally will be large in the case of ionization or electron addition. Second, these models employed empirical or adjustable parameters,[26,27] potentially distorting the true physics. Third, the calculations of Fujimori and Minami[26] only treated the smallest possible cluster ($[NiO_6]^{10-}$) as a model for the crystal. Finally, they did not include the effect of the surrounding environment on their cluster. Without more evidence, there is no reason to assume that these simple models captured all the physics necessary to assess the nature of the band gap transition.

In this work, we revisit this problem using more accurate first-principles quantum mechanics methods that were unavailable during some of those earlier studies, with the aim of shedding more light on the nature of the electronic structure of NiO. We use the ab initio complete active space self-consistent field (CASSCF)[38,39] theory to characterize the magnitude of the fundamental gap and the character of the band edges of NiO. We consider two embedded cluster models of the crystal: (a) $[NiO_6]^{10-}$ and (b) $[Ni_2O_{10}]^{16-}$ (Figure 1).

dx.doi.org/10.1021/jp500878s | J. Phys. Chem. B 2014, 118, 7963−7971

These clusters go beyond previous studies that included only one Ni atom and did not consider the magnetic coupling of Ni ions in NiO.[40] By embedding them in a point charge array, electrostatic interactions between the clusters and the surrounding crystal are taken into account. For an ionic material such as NiO, this simple embedding procedure suffices.[41] The fundamental gap can then be calculated by removing/adding an electron to simulate PES/IPES processes. The change in the energy of a system upon removing an electron is the ionization potential (IP), defined as IP = $E_{min}(N-1) - E(N)$ where $E_{min}(N-1)$ is the energy of the lowest-lying state after electron removal and $E(N)$ is the N-electron ground state. Likewise, the electron affinity (EA) corresponds to the change in the energy upon electron addition and is defined as EA = $E(N) - E_{min}(N+1)$. Here, $E_{min}(N+1)$ is the energy of the lowest-lying state after an electron is added to the system. PES and IPES measure the IP and EA of a solid, respectively. The measured PES/IPES gap is equivalent to the IP − EA gap, which is also called the QP gap E_g. It is expressed as[27]

$$E_g = E_{min}(N-1) + E_{min}(N+1) - 2E(N) \quad (1)$$

CASSCF is an appropriate theory for calculating each of these energies. This theory takes into account static electron correlation and exact exchange interactions, and optimizes both the shapes of the orbitals and the full valence CI wave function expansion coefficients. These embedded cluster calculations provide a detailed view of the wave functions as a function of charge state and provide insight into local effects in the electronic structure.

As a point of comparison, we build on our earlier DFT+U/G_0W_0 calculations,[42,43] which model the infinite crystal using periodic boundary conditions. Our DFT+U calculations employ ab initio values for U and J derived from unrestricted Hartree−Fock (UHF) theory, which contains the exact exchange we desire to include within DFT+U theory.[44,45] We use our DFT+U/G_0W_0 band gap value and electronic structure reported earlier,[42,43] along with new, detailed characterization of band edges, for comparison to our CASSCF calculations.

We validate our approach by demonstrating that our ab initio results are consistent with experiment regarding the band gap and in predicting NiO as a CT semiconductor. Additionally, these calculations unexpectedly suggest that the VBE of NiO corresponds to *partially localized* O 2p states while its CBE consists of *delocalized* Ni states, contrary to the conventional wisdom that the O 2p (Ni 3d) band is delocalized (localized).

METHODS

We performed CASSCF calculations, as implemented in the GAMESS quantum chemistry package,[48,49] on $[NiO_6]^{10-}$ and $[Ni_2O_{10}]^{16-}$ (the two clusters shown in Figure 1). These clusters were suitably embedded in an aperiodic point charge (APC) array. This embedding approach was shown to be superior to nonembedded correlated wave function methods when describing excited states of magnesium oxide, a prototypical CT metal oxide.[41] The APC array models the electrostatic potential due to the surrounding rocksalt crystal structure, which has an equilibrium lattice constant a = 4.199 Å within DFT+U theory (vide infra). The calculated a is in reasonable agreement with the experimental lattice constant, 4.180 Å.[50] The slight rhombohedral distortion in the [111] direction (0.06°) found by DFT+U was neglected in the CASSCF calculations in order to take advantage of higher symmetry in the cluster calculations. The positive point charges of the APC array immediately next to the O^{2-} anions in the clusters were replaced by "capping" Hay−Wadt Mg^{2+} effective core potentials (ECPs).[51] Capping ECPs prevent unphysical drift of electrons away from the cluster by providing the Pauli repulsion that would have been present in the crystal due to the core electrons of the bordering cations. Classical point charges do not capture this repulsion. We chose Mg^{2+} ECPs because the ionic radii of Mg^{2+} (72 pm) and Ni^{2+} (70 pm) are very similar.[52]

Prior to the replacement of the central point charges with the atoms in the cluster and capping ECPs, the APC array contained 4096 point charges in an array of 8 × 8 × 8 NiO cubic eight-atom unit cells, with O and Ni ions represented by −2e and +2e point charges, respectively. Increasing this array to 9 × 9 × 9 unit cells changed the calculated PES/IPES gap by less than 0.01 eV, so we used the smaller APC array for further analysis. The total charge on each cluster was determined assuming formal charges of +2e and −2e for Ni^{2+} and O^{2-}, respectively, according to the stoichiometry of NiO. We used the all-electron 6-31++G** basis set (contracted as (11s5p1d/4s3p1d)) for O,[53] and the Hay-Wadt VDZ basis set (contracted as (8s5p5d/3s3p2d)) for Ni, coupled with the Hay−Wadt small core ECP that represents the Ni nucleus and its 1s, 2s, and 2p core electrons.[54] Tests showed that using the small core Stuttgart ECP and its larger corresponding basis set[55] for Ni (contracted as (8s7p6d1f/5s5p3d1f)) changed the QP gap by <0.1 eV.

To mimic the final PES (IPES) levels, we removed an electron from (added an electron to) the cluster and performed CASSCF calculations on the resulting cluster ions. UHF calculations provided input wave functions for our CASSCF calculations. We used CAS(11,11), CAS(6,4), and CAS(13,11) as the active spaces for the states associated with $[NiO_6]^{9-}$, $[NiO_6]^{10-}$, and $[NiO_6]^{11-}$ calculations, respectively. (The notation CAS(n,m) means a full CI of n electrons in m orbitals is performed.) These active spaces contained 81 675−104 544, 21, and 76 230−114 312 configuration state functions (CSF), respectively. There is a range for some of these values because different symmetries and spin-states were studied in our calculations. The active spaces for $[Ni_2O_{10}]^{15-}$, $[Ni_2O_{10}]^{16-}$, and $[Ni_2O_{10}]^{17-}$ calculations were CAS(11,12), CAS(8,6), and CAS(13,12), respectively. These active spaces contained 47 190−339 768, 70−336, and 84 724−339 768 CSFs, respectively, depending on spin-state and symmetry constraints. To be consistent with our choice of active space for states with different numbers of electrons, we used the occupation numbers of active orbitals as the criterion for convergence of the active space. We included in the active space all singly occupied orbitals, all (nearly) doubly occupied orbitals with occupation numbers <1.98, and all (nearly) unoccupied orbitals with occupation numbers >0.02. We prefer this criterion rather than keeping the number of active orbitals fixed for all states. Although the latter attempts to reach consistency by keeping the variational space fixed, in reality it still leads to drastically different numbers of CSFs (and hence variational spaces) for cases with different numbers of electrons. This stems from the different numbers of ways in which different numbers of electrons can be configured for a certain set of orbitals. However, for all states with the same number of electrons, we chose the size of the active space to be that of the state with the largest active space. In all cases considered, when choosing the

dx.doi.org/10.1021/jp500878s | J. Phys. Chem. B 2014, 118, 7963−7971

(nearly) doubly occupied orbitals to be included in the active space, we tested different combinations of O 2p and Ni 3d (t_{2g}) orbitals for each state with the ultimate criterion for their inclusion in the active space being their occupation number. For calculations associated with $[NiO_6]^{9-/10-/11-}$ and $[Ni_2O_{10}]^{15-/16-/17-}$, we included the two and four singly occupied Ni 3d (e_g) orbitals, respectively, in the active space. For cases where we imposed symmetry, we chose the unoccupied (correlating) orbitals to have the same symmetries as the corresponding occupied orbitals. This choice avoids elimination of some configuration state functions on the basis of symmetry constraints.

As previously mentioned, the calculations were performed with and without imposing symmetry. For the symmetry-constrained calculations, we imposed D_{2h} and C_{2v} symmetries for $[NiO_6]^{10-}$ and $[Ni_2O_{10}]^{16-}$ clusters, respectively. D_{2h} symmetry is the highest Abelian point group symmetry possible for both of these clusters. However, as noted earlier, experiments have determined that Ni^{2+} ions couple antiferromagnetically (AFM) and ferromagnetically (FM) in [111] directions and in (111) planes, respectively.[46,47] This means that the two neighboring Ni^{2+} ions in the $[Ni_2O_{10}]^{16-}$ cluster model can be magnetically coupled either way. Therefore, the overall symmetry of the $[Ni_2O_{10}]^{16-}$ cluster should be reduced to C_{2v} in order to account for the fact that Ni^{2+} ions are not symmetry-equivalent in the AFM case. Both FM and AFM spin orderings for the two Ni^{2+} ions in the $[Ni_2O_{10}]^{16-}$ cluster were considered (as denoted in Figure 1). Note that the cluster structures are fixed, as in the G_0W_0 calculations discussed next, at the neutral bulk crystal geometries irrespective of the charge on the cluster. This is to mimic PES/IPES experiments in which the ionization/electron addition event happens on time scales much faster than those of nuclear motion.

For periodic bulk NiO calculations, we performed spin-polarized, all-electron, frozen-core, projector-augmented-wave (PAW)[56] DFT+U[23,24] and G_0W_0 calculations[30] using the VASP electronic structure package, version 5.2.2.[57,58] We employed the Dudarev et al.[59] DFT+U formalism, with the generalized gradient approximation (GGA) of Perdew–Burke–Ernzerhof (PBE)[60] as our XC functional. We used the ab initio-derived $U - J = 3.8$ eV for Ni^{2+} ions in our PBE+U calculations.[61] We employed the default PAW potentials in VASP to treat the nuclei and core electrons of the O and Ni atoms.[57,58] The O and Ni PAW potentials account for the O 1s and the Ni 1s2s2p3s3p core electrons, respectively. The PBE+U ground-state calculations provided the input one-electron wave functions and energies, as well as geometries, for the G_0W_0 calculations. The PBE+U calculations were performed with a 5 × 5 × 5 Γ-point-centered k-point mesh, with 64 bands, and a plane-wave basis kinetic energy cutoff of 700 eV on a rhombohedral unit cell that contains two O atoms and two Ni atoms. During geometry relaxation at the PBE+U level, we used Gaussian smearing for Brillouin zone integration, with a smearing width of 0.05 eV. However, we performed Brillouin zone integration using the tetrahedron method with Blöchl corrections[62,63] for the final calculations on equilibrium structures to achieve more accurate energies and densities of states (DOS). The total energy was converged to within 1 meV per atom for these settings. The directions of the initial magnetic moments on the Ni atoms were set to find states that are AFM in the [111] direction.

G_0W_0 calculations used a 4 × 4 × 4 Γ-point-centered k-point mesh, 80 empty bands, and 96 frequency points for the evaluation of the response function. At these values, the QP gap was converged to within 0.1 eV.

RESULTS AND DISCUSSION

Here we present embedded cluster CASSCF band gaps derived from the gap between the PES and IPES energy levels. We then discuss the character of these states for both PES and IPES. Finally, we compare these CASSCF predictions to those from the G_0W_0 method.

Band Gap from PES and IPES Energy Levels. We first calculate the ground-state energy $E(N)$ by performing CASSCF calculations on $[NiO_6]^{10-}$ and $[Ni_2O_{10}]^{16-}$ embedded clusters. We find, as expected, the ground state for both of these clusters to consist of doubly occupied O 2p and Ni 3d (t_{2g}), along with singly occupied Ni 3d (e_g) orbitals. For $[Ni_2O_{10}]^{16-}$, the global energy minimum is predicted to be the AFM state, but it is only 2 meV below the ground state of the FM manifold.

In what follows, we calculate E_g from the many-electron total energies of the states associated with the $[NiO_6]^{9-/10-/11-}$ and $[Ni_2O_{10}]^{15-/16-/17-}$ embedded clusters. These levels correspond to several states measured by PES and IPES experiments. Figure 2 displays all the calculated PES and IPES levels, namely

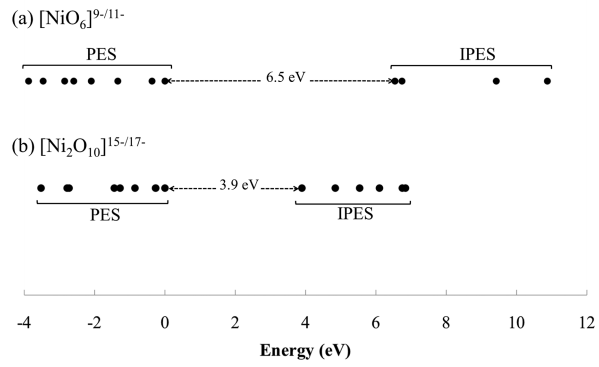

Figure 2. PES and IPES energy levels calculated for (a) $[NiO_6]^{10-}$ and (b) $[Ni_2O_{10}]^{16-}$ clusters. For PES, the energies in this plot are the total energies of the $N - 1$ system, referenced to the minimum energy state (expressed as $E = E_{min}(N-1) - E(N-1)$), whereas IPES energies are the modified total energies of the $N + 1$ system (expressed as $E = E_g + [E(N+1) - E_{min}(N+1)]$. See text for further explanation.

symmetry- and non-symmetry-imposed solutions, as well as FM and AFM spin orderings of the Ni atoms in the $[Ni_2O_{10}]^{15-/16-/17-}$ embedded cluster. To make these energy levels directly comparable to those of experimental PES and IPES spectra, we express the energy E of each PES state in Figure 2 as

$$E_{PES} = E_{min}(N-1) - E(N-1) \quad (2)$$

where N is the number of electrons in the neutral cluster, $E(N-1)$ is the energy of a state associated with the ionized cluster, and $E_{min}(N-1)$ is the lowest energy level associated with the ionized cluster (i.e., the lowest energy ionized state that effectively defines the VBE). For IPES, we express the corresponding energy as

$$E_{IPES} = E_g + [E(N+1) - E_{min}(N+1)] \quad (3)$$

Here, $E(N+1)$ is the energy of a state when an electron is added to the cluster, $E_{min}(N+1)$ is the energy of the lowest-

dx.doi.org/10.1021/jp500878s | J. Phys. Chem. B 2014, 118, 7963–7971

lying state when an electron is added to the cluster, and E_g is defined by eq 1.

The calculated PES and IPES energy levels yield E_g of 6.5 and 3.9 eV for $[NiO_6]^{9-/11-}$ and $[Ni_2O_{10}]^{15-/17-}$, respectively. The reduction in band gap is in accordance with the well-known quantum size effect.[64] Experiments measure a gap of 3.4−4.6 eV.[17] Thus, while the $[NiO_6]^{9-/11-}$ cluster calculations overestimate the PES/IPES gap, the $[Ni_2O_{10}]^{15-/17-}$ cluster calculations agree with experiment. Unfortunately, because of the factorial scaling of CASSCF calculations, we cannot explore larger clusters to check convergence of the gap with respect to cluster size. Nevertheless, these cluster calculations allow us to explore the character of the states formed upon electron removal or addition, as we discuss next.

Character of PES States. As we shall see below, both cluster models indicate that the valence PES spectrum of NiO consists of hole states with both O 2p and Ni 3d (t_{2g})/O 2p hybrid character. However, the edge of the PES spectrum consists only of states with predominantly O 2p character. $[NiO_6]^{9-}$ calculations do not give any localized solutions, whereas for $[Ni_2O_{10}]^{15-}$ the edge consists of a localized state centered around two O atoms.

$[NiO_6]^{9-}$ Cluster Model. Figure 3 displays electron density difference plots for each of the PES states of the cluster, shown ordered by electron binding energy. The change in charge density when an electron is removed can be used to determine the character of the remaining hole produced by the PES process. The changes we observe show that the edge of the spectrum consists of states (^{2}A and ^2A_g) in which the hole has a predominant O 2p and, to a lesser extent, Ni 3d (e_g) character when an electron is removed from the $[NiO_6]^{10-}$ cluster. The hole has a more prominent Ni 3d (t_{2g}) character compared to O 2p in the few states that lie immediately below the edge (^{4}A, $^4B_{1g}$, $^4B_{2g}$, and $^4B_{3g}$). However, the holes in the rest of the $[NiO_6]^{9-}$ states either have O 2p character ($^{2,4}B_{1u}$, $^{2,4}B_{2u}$, $^{2,4}B_{3u}$, and ^4A_g) or a hybrid of Ni 3d (t_{2g}) and O 2p ($^2B_{1g}$, $^2B_{2g}$, $^2B_{3g}$, and $^{2,4}A_u$). Overall, the O 2p character is more prevalent for the holes in the $[NiO_6]^{9-}$ states close to the edge of the PES spectrum. Removing an electron from an O 2p orbital requires less energy than removing one from a Ni 3d orbital, as expected because of the excess negative charge on the oxide anion in NiO. This analysis confirms the experimental observations[19,29] and our previous theoretical findings[61] that the holes near the VBE in p-type NiO have mostly O 2p character.

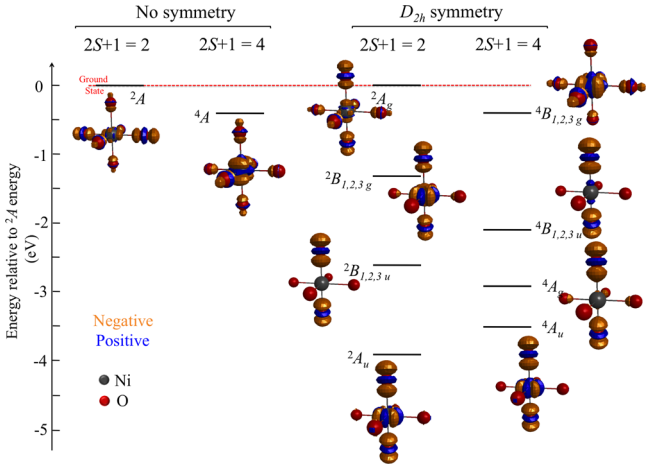

Figure 3. Energy levels of the $[NiO_6]^{9-}$ cluster modeling hole states formed in photoemission of NiO. We show cases without symmetry constraints and with D_{2h} symmetry imposed. Each case considers states with both possible spin multiplicities 2 and 4. Charge density difference plots next to each state correspond to $\rho([NiO_6]^{9-}) - \rho([NiO_6]^{10-})$, i.e., the hole density. The contour value for the charge density ρ difference plots is 0.01 electrons per bohr^3. We used the MacMolPlt software[65] for visualization of the clusters, charge density differences, and molecular orbitals in all figures.

The ordering of the $[NiO_6]^{9-}$ states in Figure 3 is also noteworthy. Although generally the holes are primarily O 2p in character, holes on Ni^{2+} are energetically more favorable than those on O^{2-} when removing minority spin electrons. This is evident from the ordering of the $^4B_{1u}$ and $^4B_{1g}$ states. Such ordering is due to the stabilization gained from the larger exchange interaction between the singly occupied electrons in Ni^{3+} compared to that in an O^{1-}/Ni^{2+} combination. A similar argument can explain the ordering of $^4B_{1u}$ and $^2B_{1u}$ states and that of ^4A_u and ^2A_u states. In these cases, more exchange energy is gained when the singly occupied electron on O has the same spin as the Ni d (e_g) electrons. In sum, the character of the $[NiO_6]^{9-}$ states and their arrangement is fairly consistent with measurements and physical intuition despite the gross overestimation of the gap calculated within this cluster model.

$[Ni_2O_{10}]^{15-}$ Cluster Model. Figure 4 displays the corresponding electron density difference plots for the larger cluster, again ordered by electron binding energy. Evaluation of density differences between $[Ni_2O_{10}]^{16-}$ and $[Ni_2O_{10}]^{15-}$ embedded clusters reveals that the holes associated with the majority of $[Ni_2O_{10}]^{15-}$ states again have largely O 2p character, consistent with experiment.[17,19,29] This includes the ^{2}A state at the edge and the ^{4}A and $^4B_1$ states immediately below it. Only for the ^{6}A and $^2A_1$ states does the Ni 3d (t_{2g}) character of the hole become significant. These states lie well below the edge at ∼ −1.4 and −2.7 eV, respectively. The calculations performed with or without symmetry constraints both suggest that the VBE state of $[Ni_2O_{10}]^{15-}$ is fairly localized in addition to having primarily O 2p character. It could be argued that the somewhat different environments of the eight *outer* and two *inner* O ions may prevent the hole from delocalization (outer O ions

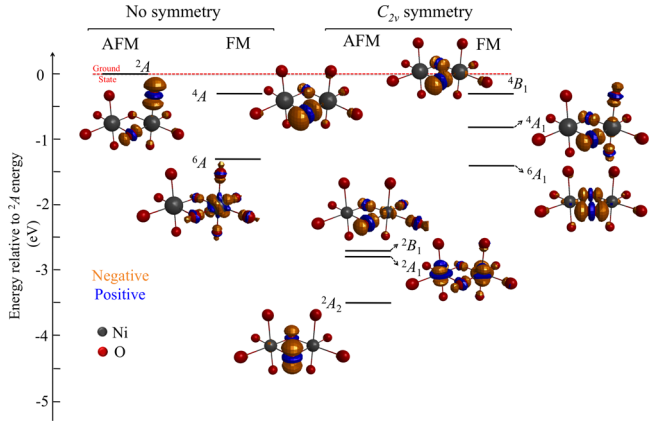

Figure 4. Energy levels of the $[Ni_2O_{10}]^{15-}$ cluster modeling hole states formed in photoemission of NiO. We show cases without symmetry constraints and with C_{2v} symmetry imposed. Each case considers states with both possible AFM and FM spin configurations for the two Ni^{2+} ions. The charge density difference plots next to each state correspond to $\rho([Ni_2O_{10}]^{15-}) - \rho([Ni_2O_{10}]^{16-})$, i.e., the hole density. The contour value for the charge density plots is 0.01 electrons per bohr^3.

dx.doi.org/10.1021/jp500878s | J. Phys. Chem. B 2014, 118, 7963−7971

neighbor only one Ni ion, as opposed to inner O ions, which are adjacent to two Ni ions). But our cluster choice does not give rise to any effect that could prevent the hole delocalization among the outer O ions. Despite this fact, the hole associated with state ^{2}A, which is the ground state of $[Ni_2O_{10}]^{15-}$, has a prominent presence on only one of the eight outer O ions (Figure 4). This is a strong indication for the preference of the hole to localize. To our knowledge, such localization had not been identified in previous calculations.

A closer look at the occupation numbers associated with the active orbitals in the different states of $[Ni_2O_{10}]^{15-}$ cluster shows that the most significant correlating orbitals are the (nearly) unoccupied orbitals rather than the singly occupied Ni 3d (e_g) orbitals in the active space. By and large these singly occupied orbitals stay singly occupied, while the (nearly) unoccupied orbitals optimize to be the antibonding orbitals of the (nearly) doubly occupied orbitals. For each state, the character of these orbitals is O 2p, Ni 3d (t_{2g}), or a hybrid of the two, depending on the character of the hole associated with that state.

Two differences between $[NiO_6]^{9-}$ and $[Ni_2O_{10}]^{15-}$ states underline the importance of considering the larger cluster. First, the localized character of the VBE state in $[Ni_2O_{10}]^{15-}$ does not appear in the $[NiO_6]^{9-}$ results. Second, in contrast to the $[Ni_2O_{10}]^{15-}$ embedded cluster results, the VBE states of $[NiO_6]^{9-}$ include some Ni 3d (e_g) character that are in a highly stable configuration in Ni^{2+} ions. Removing an electron from a Ni^{2+} ion, either from the e_g orbitals (reducing favorable exchange interactions) or the t_{2g} orbitals (bound most strongly), requires much more energy than removing one from O^{2-}. Consequently, the predicted band gap in the smaller cluster is larger (Figure 2) because of the difference in predicted character of the VBE. The larger cluster, with its dominant O 2p character at the VBE, is a more realistic model of NiO PES spectrum and produces a physically realistic band gap as result.

Character of IPES States. *$[NiO_6]^{11-}$ Cluster Model.* We modeled the IPES spectrum by adding an electron to the electrostatically embedded $[NiO_6]^{10-}$ cluster. Charge density difference plots show that the states at the CBE of the resulting spectrum are highly delocalized (Figure 5, states ^{2,4}A, $^{2,4}B_{1u}$, $^{2,4}B_{2u}$, and $^{2,4}B_{3u}$). However, these plots do not identify the character of the added electron. To get a more detailed picture, we consider the orbitals involved after adding an electron (Figure 5 inset). Before the electron is added to $[NiO_6]^{10-}$, the singly occupied orbitals are primarily Ni 3d (e_g) in character. These orbitals can potentially host an additional electron that has its spin opposite to the electrons that already occupy them. But remarkably, after an opposite-spin electron is added to produce low-spin $[NiO_6]^{11-}$, these two orbitals remain singly occupied (^{2}A and $^2B_{1,2,3u}$ states in Figure 5). The additional electron occupies another orbital with primarily Ni 4p character instead of filling one of the empty states in the Ni 3d (e_g) orbitals or occupying a Ni 4s state, which is expected to be lower in energy than the 4p state. This result already strongly hints that the cluster is simply too small to properly capture the physics of electron addition. The localized states at higher energies correspond to an additional electron in the Ni 3d (e_g) orbitals. The delocalized states lie lower in energy than those of the localized states, indicating the electron's preference to be delocalized. Because the Ni 4p states are high-lying in energy, this also contributes to the gross overestimation of the QP gap.

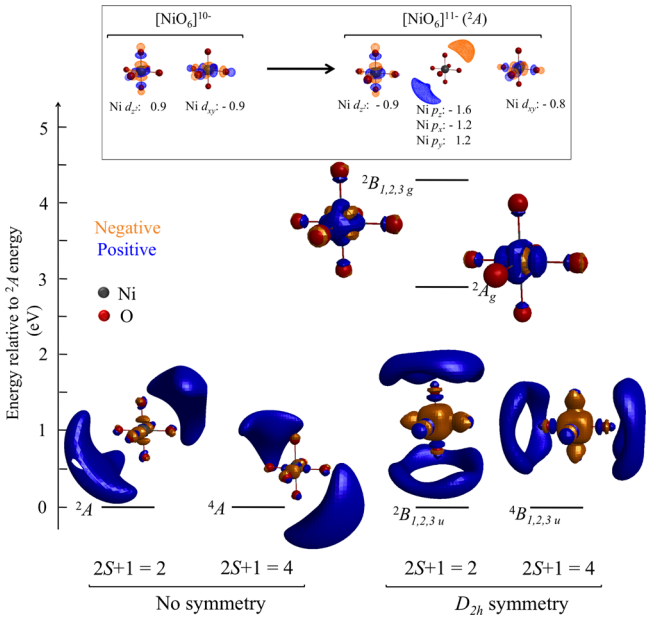

Figure 5. Energy levels associated with $[NiO_6]^{11-}$. The charge density difference plots correspond to $\rho([NiO_6]^{11-}) - \rho([NiO_6]^{10-})$, with the contour value of 0.0005 electrons per bohr^3 for the states below 2 eV and 0.01 electrons per bohr^3 for the states above 2 eV. The contour value is much smaller than that for the hole states in PES because of the delocalized nature of the electron states, which leads to smaller charge density at each point in space. To illustrate how we characterized the delocalized states, the inset shows the singly occupied molecular orbitals before and after adding an electron for the case of the ^{2}A state. Each molecular orbital is labeled by its atomic orbitals (AOs) that have coefficients >0.4, along with the corresponding coefficients. In this specific case, O-centered AOs do not contribute.

As shown next, the larger cluster has a very different character for the CBE states.

$[Ni_2O_{10}]^{17-}$ Cluster Model. Electron density difference plots indicate that, similar to $[NiO_6]^{11-}$, the ground state of $[Ni_2O_{10}]^{17-}$ is delocalized (Figure 6, state ^{2}A). The added electron has its spin opposite to two (four) of the four electrons in the singly occupied Ni 3d (e_g) orbitals of $[Ni_2O_{10}]^{16-}$ in the AFM (FM) spin configurations. Hence, it can potentially occupy one of these orbitals and form a doubly occupied Ni 3d (e_g) orbital. However, inspection of the relevant orbitals shows that the additional electron does not occupy any of the Ni 3d (e_g) orbitals (Figure 6 inset); rather, it singly occupies a new, previously unoccupied orbital. Other than this now singly occupied orbital, the other (nearly) unoccupied orbitals in the active space act as correlating orbitals for the (nearly) doubly occupied orbitals, which have primarily O 2p character. The Ni 3d (e_g) orbitals remain singly occupied. This is consistent with the role that the (nearly) unoccupied orbitals of the active space play in $[Ni_2O_{10}]^{15-}$. In the lowest-lying states (^{2}A, ^{4}A, and $^4A_1$), which corresponds to the CBE of the IPES spectrum, and in the states $^2A_1$ and $^2A_2$, this singly occupied orbital has a predominant Ni 4s character hybridized with Ni 4p and Ni 3d (e_g). For the higher-lying $^4B_1$ and $^2B_1$ states, Ni 4p characteristics become prominent and Ni 4s character disappears, consistent with the former's expected higher relative energy. Ni 3d (e_g) character still has a significant presence in these states. Whenever Ni 4s and 4p characters are substantial,

dx.doi.org/10.1021/jp500878s | J. Phys. Chem. B 2014, 118, 7963−7971

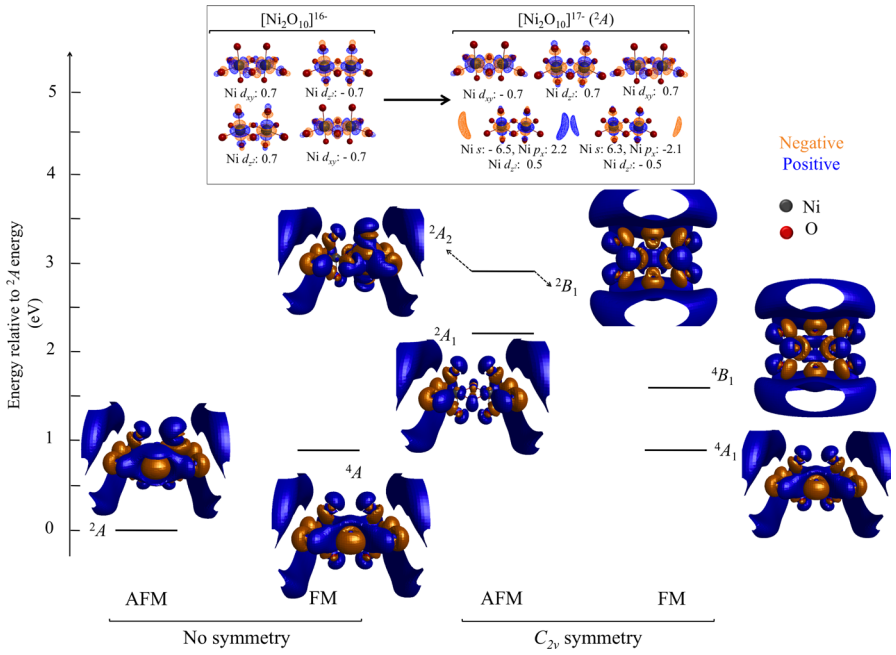

Figure 6. Energy levels of $[Ni_2O_{10}]^{17-}$. The charge density difference plots correspond to $\rho([Ni_2O_{10}]^{17-}) - \rho([Ni_2O_{10}]^{16-})$, with the contour value of 0.0005 electrons per bohr^3. The contour value is much smaller than that for the hole states in PES because of the delocalized nature of the electron states, which leads to smaller charge density at each point in space. As an example of how we determined the character of the delocalized states, the inset shows the singly occupied molecular orbitals before and after adding an electron for the case of the ^{2}A state. Each molecular orbital is labeled by its AOs that have coefficients >0.4, along with the corresponding coefficients.

some hybridization also occurs with empty O 3s and 3p orbitals, respectively.

$[NiO_6]^{11-}$ and $[Ni_2O_{10}]^{17-}$ energy levels differ in that there are no localized states at higher energies for the latter. Also, the added electrons in low-lying states of $[Ni_2O_{10}]^{17-}$ have primarily Ni 4s character in contrast to those in $[NiO_6]^{11-}$, for which Ni 4p is prominent. Occupying the Ni 4s is a much more physically sensible result because it should be lower-lying than the Ni 4p and it allows for more favorable exchange interactions to form between the 4s and the Ni 3d electrons. This is undoubtedly why the larger cluster gives rise to a sensible band gap as well.

Overall, our calculations show that the embedded $[Ni_2O_{10}]^{15-/16-/17-}$ clusters model the PES/IPES measurements more capably than the smaller $[NiO_6]^{9-/10-/11-}$ calculations. These calculations produce a QP gap of 3.9 eV, in good agreement with experiment.[17] They further indicate that NiO is a CT semiconductor. The valence band edge of the PES spectrum corresponds to a fairly localized, dominantly O 2p state. In contrast, the lowest edge of the IPES spectrum has a hybrid Ni 4s/Ni 4p/Ni 3d (e_g) character and is highly delocalized. Next we compare the results of these finite-sized embedded cluster calculations with those of periodically infinite bulk crystal calculations.

Character of States from G_0W_0 Theory. We performed G_0W_0 calculations using PBE+U ($U - J$ = 3.8 eV) eigenvalues and wave functions as input. This method was shown to be reliable for predicting QP properties for several late TMOs.[61,66,67] The G_0W_0 QP gap is 3.6 eV, which falls within the experimental range, 3.4−4.6 eV.[17] By contrast, ground-state calculations with PBE+U without G_0W_0 find an eigenvalue gap of 2.6 eV,[61] which underestimates the gap by at least 1 eV. This demonstrates the necessity of using G_0W_0 to study the electronic structure of NiO when modeling the infinite crystal using periodic boundary conditions. As Figure 7 illustrates, the VBE has both O 2p and Ni 3d character, while the CBE

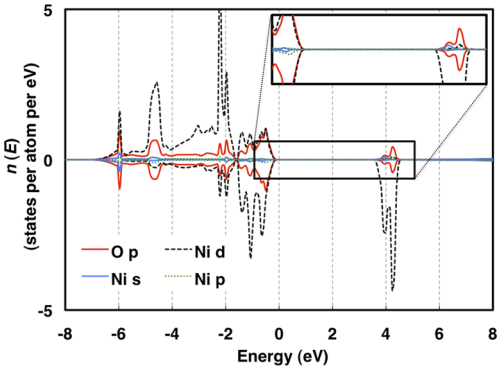

Figure 7. Projected DOS calculated by PBE+U/G_0W_0 for NiO. Positive and negative DOS correspond to majority and minority spin states, respectively. The inset shows the character of the band edges in more detail. The Fermi level is set to the zero of energy.

contains mostly Ni 3d states. Ni 4s states have a small presence at the CBE and states with hybrid Ni 4p, Ni 3d, and O 3p character appear at energies around 0.3 eV above the CBE.

The presence of O 2p character at the edge of the G_0W_0 valence band is consistent with our $[Ni_2O_{10}]^{15-}$ cluster calculations. The Ni 3d states appear around 1.4 eV below the lowest energy (band edge) state of $[Ni_2O_{10}]^{15-}$ (state ^{6}A in Figure 4). In the G_0W_0 results, these states appear at 0.7, 1.1, and 1.4 eV below the VBE. The extra states at lower binding energy are presumably due to the broadening of Ni 3d bands in the periodic G_0W_0 model, which also induces increased hybridization with the O 2p states closer to VBE. Such effects are smaller in the cluster model because of the finite extent of

dx.doi.org/10.1021/jp500878s | J. Phys. Chem. B 2014, 118, 7963−7971

the cluster. As for the IPES states, both $[Ni_2O_{10}]^{17-}$ and G_0W_0 calculations indicate the presence of Ni 3d states in the vicinity of the CBE. Ni 4s character is also present in both of these calculations; however, it is much more prevalent in the $[Ni_2O_{10}]^{17-}$ cluster calculations. The CBE associated with G_0W_0 is devoid of Ni 4p states. This is a notable difference between $[Ni_2O_{10}]^{17-}$ calculations and G_0W_0. However, this disappearance of Ni 4p states from a finite cluster model to G_0W_0, which treats the infinite crystal, is consistent with the decreased relative importance of Ni 4p states when moving from the smaller $[NiO_6]^{11-}$ cluster to $[Ni_2O_{10}]^{17-}$. Overall, our G_0W_0 calculations are in qualitative agreement with cluster calculations. They both describe NiO as a wide-gap CT semiconductor. Complete quantitative agreement of the gap and the position of the peaks cannot be expected because, aside from employing different physical approximations, G_0W_0 treats the infinite crystal limit.

CONCLUSIONS

We evaluated the PES/IPES gap in NiO and revisited identification of the characters of its band edges using embedded cluster CASSCF and periodic G_0W_0 calculations. These calculations agree in several ways, provided the larger cluster model is employed. This agreement and the agreement with experimental results lend credence to the appropriateness of our cluster model for treating NiO electronic structure. Both theories result in band gaps within the experimental range. They predict that O 2p states are prevalent at the VBE of NiO and that Ni states dominate the CBE; in the cluster calculations, Ni 4s, Ni 4p, and Ni 3d each contribute to the CBE, whereas in the periodic calculations, Ni 3d character is more significant.

Our model removes some assumptions made in previous studies.[26,27] Our cluster calculations show the importance of going beyond the smallest possible cluster ($[NiO_6]^{10-}$) to understand the nature of the energy levels that correspond to the PES and IPES spectra. In addition, eliminating empirical or adjustable parameters while including static correlation and optimizing the shapes of the orbitals involved in the processes produced excellent agreement with experiment. The success of our calculations demonstrates that APC embedded CASSCF theory can potentially be used to study localized excited states and other important NiO properties, such as polaronic transport. These properties are critical for assessing the potential of a material for use in solar energy applications. The possibility of calculating such properties highlights some advantages of embedded correlated wave function theories over G_0W_0.

We find that the holes at the edge of the PES spectrum of NiO have a predominant O 2p character, in agreement with experiment.[29] This is in contrast to earlier cluster calculations that described the VBE as having a hybrid Ni 3d (t_{2g})/O 2p character.[26,27] We also find that the VBE corresponds to a somewhat localized state. Previous calculations did not describe the spatial extent of the holes at the VBE.[26,27,40] Our CASSCF calculations show that the IPES edge involves a delocalized state, with the additional electron occupying an orbital that is largely Ni 4s in character but hybridized with Ni 3d (e_g) and Ni 4p. This contradicts the conventional wisdom that localized Ni 3d (e_g) states dominate the CBE.[26,27]

In sum, according to our calculated PES and IPES energy spectra, NiO is a CT material with a gap of 3.6−3.9 eV, in agreement with the experimental range of 3.4−4.6 eV.[17] The different characters of the valence and conduction band edges may lead to low electron−hole recombination.[18] The localized nature of the states at the VBE shows that transport properties of holes in NiO may be properly treated with a small polaron model[68] and that hole mobility is likely to be low. By contrast, the delocalized character at the CBE may be beneficial for efficient electron transport through the material. However, transport studies must go beyond our single-structure calculations and assess the spatial character of holes and electrons in the presence of geometric distortion and coupling between localized states. Despite its favorable CT property and possible gains from delocalized conduction band electronic states, the band gap of NiO is too large to efficiently absorb solar energy. However, other work has shown that this problem can be circumvented by tuning the gap through alloying NiO with other metal oxides.[42,61]

AUTHOR INFORMATION

Corresponding Author

*E-mail: eac@princeton.edu.

Notes

The authors declare no competing financial interest.

ACKNOWLEDGMENTS

E.A.C. thanks the U.S. Department of Energy, Basic Energy Sciences for funding this project. A portion of the research was performed using EMSL, a national scientific user facility sponsored by the Department of Energy's Office of Biological and Environmental Research and located at Pacific Northwest National Laboratory. Research leading to these results also received funding from the European Union Seventh Framework Programme (FP7/2007-2013) under Grant Agreement [254227] to M.C.T.

REFERENCES

(1) Bak, T.; Nowotny, J.; Rekas, M.; Sorrell, C. C. *Int. J. Hydrogen Energy* **2002**, *27*, 991−1022.
(2) Sivula, K.; Le Formal, F.; Grätzel, M. *ChemSusChem* **2011**, *4*, 432−449.
(3) Powar, S.; Wu, Q.; Weidelener, M.; Nattestad, A.; Hu, Z.; Mishra, A.; Bäuerle, P.; Spiccia, L.; Cheng, Y.-B.; Bach, U. *Energy Environ. Sci.* **2012**, *5*, 8896−8900.
(4) Irwin, M. D.; Buchholz, D. B.; Hains, A. W.; Chang, R. P. H.; Marks, T. J. *Proc. Natl. Acad. Sci. U.S.A.* **2008**, *105*, 2783−2787.
(5) Nattestad, A.; Ferguson, M.; Kerr, R.; Cheng, Y.-B.; Bach, U. *Nanotechnology* **2008**, *19*, 295304.
(6) Zou, Z.; Ye, J.; Sayama, K.; Arakawa, H. *Nature (London, U.K.)* **2001**, *414*, 625−627.
(7) Mori, S.; Fukuda, S.; Sumikura, S.; Takeda, Y.; Tamaki, Y.; Suzuki, E.; Abe, T. *J. Phys. Chem. C* **2008**, *112*, 16134−16139.
(8) Morandeira, A.; Fortage, J.; Edvinsson, T.; LePleux, L.; Blart, E.; Boschloo, G.; Hagfeldt, A.; Hammarstrom, L.; Odobel, F. *J. Phys. Chem. C* **2008**, *112*, 1721−1728.
(9) Zhu, H.; Hagfeldt, A.; Boschloo, G. *J. Phys. Chem. C* **2007**, *111*, 17455−17458.
(10) Borgström, M.; Blart, E.; Boschloo, G.; Mukhtar, E.; Hagfeldt, A.; Hammarström, L.; Odobel, F. *J. Phys. Chem. B* **2005**, *109*, 22928−22934.
(11) Ji, Z.; Natu, G.; Huang, Z.; Kokhan, O.; Zhang, X.; Wu, Y. *J. Phys. Chem. C* **2012**, *116*, 16854−16863.
(12) He, J.; Lindström, H.; Hagfeldt, A.; Lindquist, S.-E. *Sol. Energy Mater. Sol. Cells* **2000**, *62*, 265−273.
(13) Nattestad, A.; Mozer, A. J.; Fischer, M. K. R.; Cheng, Y.-B.; Mishra, A.; Bäuerle, P.; Bach, U. *Nat. Mater.* **2010**, *9*, 31−5.

(14) He, J.; Lindström, H.; Hagfeldt, A.; Lindquist, S. *J. Phys. Chem. B* **1999**, *103*, 8940−8943.
(15) Mizoguchi, Y.; Fujihara, S. *Electrochem. Solid-State Lett.* **2008**, *11*, K78−K80.
(16) Morandeira, A.; Boschloo, G.; Hagfeldt, A.; Hammarström, L. *J. Phys. Chem. B* **2005**, *109*, 19403−19410.
(17) Hüfner, S. *Adv. Phys.* **1994**, *43*, 183−356.
(18) Liao, P.; Carter, E. A. *Chem. Soc. Rev.* **2013**, *42*, 2401−2422.
(19) Kuiper, P.; Kruizinga, G.; Ghijsen, J.; Sawatzky, G. A.; Verweij, H. *Phys. Rev. Lett.* **1989**, *62*, 221−224.
(20) Mott, N. F. *Proc. Phys. Soc., London, Sect. A* **1949**, *62*, 416−422.
(21) Hubbard, J. *Proc. R. Soc. London, Ser. A* **1963**, *276*, 238−257.
(22) Terakura, K.; Oguchi, T.; Williams, A. R.; Kübler, J. *Phys. Rev. B* **1984**, *30*, 4734−4747.
(23) Anisimov, V. I.; Zaanen, J.; Anderson, O. K. *Phys. Rev. B* **1991**, *44*, 943−954.
(24) Anisimov, V. I.; Solovyev, I. V.; Korotin, M. A.; Czyżyk, M. T.; Sawatzky, G. A. *Phys. Rev. B* **1993**, *48*, 16929−16934.
(25) Bengone, O.; Alouani, M.; Blöchl, P.; Hugel, J. *Phys. Rev. B* **2000**, *62*, 16392−16401.
(26) Fujimori, A.; Minami, F. *Phys. Rev. B* **1984**, *30*, 957−971.
(27) Zaanen, J.; Sawatzky, G. A.; Allen, J. W. *Phys. Rev. Lett.* **1985**, *55*, 418−421.
(28) Hüfner, S.; Steiner, P.; Sander, I.; Reinert, F.; Schmitt, H. *Z. Phys. B: Condens. Matter* **1992**, *86*, 207−215.
(29) Van Elp, J.; Eskes, H.; Kuiper, P.; Sawatzky, G. A. *Phys. Rev. B* **1992**, *45*, 1612−1622.
(30) Hedin, L. *Phys. Rev.* **1965**, *139*, A796−A823.
(31) Szabo, A.; Ostlund, N. S. *Modern Quantum Chemistry: Introduction to Advanced Electronic Structure Theory*; Dover Publications: Mineola, NY, 1996.
(32) Heyd, J.; Scuseria, G. E.; Ernzerhof, M. *J. Chem. Phys.* **2003**, *118*, 8207.
(33) Heyd, J.; Scuseria, G. E.; Ernzerhof, M. *J. Chem. Phys.* **2006**, *124*, 219906.
(34) Jiang, H.; Gomez-Abal, R. I.; Rinke, P.; Scheffler, M. *Phys. Rev. B* **2010**, *82*, 045108.
(35) Rödl, C.; Fuchs, F.; Furthmüller, J.; Bechstedt, F. *Phys. Rev. B* **2009**, *79*, 235114.
(36) Faleev, S. V.; van Schilfgaarde, M.; Kotani, T. *Phys. Rev. Lett.* **2004**, *93*, 126406.
(37) Madsen, G. K. H.; Novák, P. *Europhys. Lett.* **2005**, *69*, 777−783.
(38) Roos, B. O.; Taylor, P. R. *Chem. Phys.* **1980**, *48*, 157−173.
(39) Roos, B. O. In *Advances in Chemical Physics: Ab Initio Methods in Quantum Chemistry Part 2*; Lawley, K. P., Ed.; John Wiley & Sons Ltd.: New York, 1987; Vol. *69*, pp 399−445.
(40) Domingo, A.; Rodríguez-Fortea, A.; Swart, M.; de Graaf, C.; Broer, R. *Phys. Rev. B* **2012**, *85*, 1−15.
(41) Kanan, D. K.; Sharifzadeh, S.; Carter, E. A. *Chem. Phys. Lett.* **2012**, *519*−*520*, 18−24.
(42) Caspary Toroker, M.; Carter, E. A. *J. Mater. Chem. A* **2013**, *1*, 2474.
(43) Caspary Toroker, M.; Kanan, D. K.; Alidoust, N.; Isseroff, L. Y.; Liao, P.; Carter, E. A. *Phys. Chem. Chem. Phys.* **2011**, *13*, 16644−16654.
(44) Mosey, N.; Carter, E. A. *Phys. Rev. B* **2007**, *76*, 155123.
(45) Mosey, N. J.; Liao, P.; Carter, E. A. *J. Chem. Phys.* **2008**, *129*, 014103.
(46) Slack, G. a. *J. Appl. Phys.* **1960**, *31*, 1571.
(47) Messick, L.; Walker, W. C.; Glosser, R. *Phys. Rev. B* **1972**, *6*, 3941−3949.
(48) Schmidt, M. W.; Baldridge, K. K.; Boatz, J. A.; Elbert, S. T.; Gordon, M. S.; Jensen, J. H.; Koseki, S.; Matsunaga, N.; Nguyen, K. A.; Su, S.; Windus, T. L.; Dupuis, M.; Montgomery, J. A. *J. Comput. Chem.* **1993**, *14*, 1347−1363.
(49) Gordon, M. S.; Schmidt, M. W. In *Theory and Applications of Computational Chemistry: The First Forty Years*; Dykstra, C. E., Frenking, G., Kim, K. S., Scuseria, G. E., Eds.; Elsevier: Amsterdam, 2005; pp 1167−1189.
(50) Fiévet, F.; Germi, P.; de Bergevin, F.; Figlarz, M. *J. Appl. Crystallogr.* **1979**, *12*, 387−394.
(51) Wadt, W. R.; Hay, P. J. *J. Chem. Phys.* **1985**, *82*, 284−298.
(52) Shannon, R. D.; Prewitt, C. T. *Acta Crystallogr., Sect. B: Struct. Crystallogr. Cryst. Chem.* **1969**, *25*, 925−946.
(53) Hehre, W. J.; Ditchfield, R.; Pople, J. A. *J. Chem. Phys.* **1972**, *56*, 2257−2261.
(54) Hay, P. J.; Wadt, W. R. *J. Chem. Phys.* **1985**, *82*, 299−310.
(55) Dolg, M.; Wedig, U.; Stoll, H.; Preuss, H. *J. Chem. Phys.* **1987**, *86*, 866.
(56) Blöchl, P. E. *Phys. Rev. B* **1994**, *50*, 17953−17979.
(57) Kresse, G.; Furthmüller, J. *Comput. Mater. Sci.* **1996**, *6*, 15−50.
(58) Kresse, G.; Hafner, J. *Phys. Rev. B* **1993**, *47*, 558−561.
(59) Dudarev, S. L.; Botton, G. A.; Savrasov, S. Y.; Humphreys, C. J.; Sutton, A. P. *Phys. Rev. B* **1998**, *57*, 1505−1509.
(60) Perdew, J. P.; Burke, K.; Ernzerhof, M. *Phys. Rev. Lett.* **1996**, *77*, 3865−3868.
(61) Alidoust, N.; Caspary Toroker, M.; Keith, J. A.; Carter, E. A. *ChemSusChem* **2014**, *7*, 195−201.
(62) Jepson, O.; Andersen, O. K. *Solid State Commun.* **1971**, *9*, 1763−1767.
(63) Blöchl, P. E.; Jepsen, O.; Andersen, O. K. *Phys. Rev. B* **1994**, *49*, 16223−16233.
(64) Khanna, S. N.; Castleman, A. W. *Quantum Phenomena in Clusters and Nanostructures*; Springer: Berlin, 2003; p 42.
(65) Bode, B. M.; Gordon, M. S. *J. Mol. Graphics Modell.* **1998**, *16*, 133−138.
(66) Liao, P.; Carter, E. A. *Phys. Chem. Chem. Phys.* **2011**, *13*, 15189−15199.
(67) Isseroff, L. Y.; Carter, E. A. *Phys. Rev. B* **2012**, *85*, 235142.
(68) Holstein, T. *Ann. Phys. (N.Y., NY, U.S.)* **1959**, *8*, 343−389.